Available online at www.sciencedirect.com
ScienceDirect
International Journal of Heat and Mass Transfer 50 (2007) 3507–3520
International Journal of HEAT and MASS TRANSFER
www.elsevier.com/locate/ijhmt

A numerical study on the fluid flow and heat transfer around a circular cylinder near a moving wall

H.S. Yoon [a,*], J.B. Lee [b], H.H. Chun [a]

[a] Advanced Ship Engineering Research Center, Pusan National University, San 30, Jang Jeon Dong, Geum Jeong Gu, Busan 609-735, Republic of Korea
[b] Department of Naval Architecture and Ocean Engineering, Pusan National University, San 30, Jang Jeon Dong, Geum Jeong Gu, Busan 609-735, Republic of Korea

Received 17 August 2006; received in revised form 6 January 2007
Available online 13 March 2007

Abstract

The present study numerically investigates two-dimensional laminar fluid flow and heat transfer past a circular cylinder near a moving wall. For the purpose of a careful analysis of the modification of flow and thermal fields around a cylinder by a moving wall, numerical simulations to calculate the fluid flow and heat transfer past a circular cylinder are performed for different Reynolds numbers of 100, 140 and 180 and a fixed Prandtl numbers of 0.7 (air) in the range of $0.1 \leqslant G/D \leqslant 4$, where G/D is the ratio of the gap between the cylinder and a moving wall, G and the cylinder diameter, D. The present study reports the detailed information of flow and thermal quantities on the cylinder surface at different gap ratios. As the gap ratio decreases, the vortex shedding formed in the wake is suppressed and the oscillating amplitude of lift coefficient decreases. Thus the drag, lift coefficients and Nusselt number representing the fluid flow and heat transfer characteristics also vary as a function of the gap ratio with the dependence of Reynolds number.

1. Introduction

This study aims at a careful analysis of the modification of flow and thermal fields around a cylinder by the moving wall placed below the bottom of a cylinder. An example of such a flow is the flow past a vehicle and a submarine moving near a wall.

In the unbounded condition, the phenomenon of flow separation, bluff body wake and prediction of heat transfer from a cylinder have been intensely studied for a long time because of their fundamental significance in flow physics and their practical importance in aerodynamic and heat transfer applications [1–12]. The generation and evolution of vortical structures in the wake region have a big effect on the drag, heat transfer, flow-induced vibration and noise problems.

The flow around a cylinder near to a stationary plane wall can be considered as the similarly relevant problem to the present topic. As well known, the effect of a stationary plane wall on the flow around a cylinder is mainly classified into following three factors [13]. First, the no-penetration condition on a stationary wall prevents the expansion of the flow and produces the repulsive force from a stationary wall. Second, the non-uniform profile of free-stream velocity is induced by a stationary wall and as a result a velocity shear gives an asymmetric influence on the cylinder. Third, the no-slip conditions on the wall distort the flow in the wake behind the cylinder and separate the boundary layer from a stationary plane wall. Thus, the combination of the vorticity shed from the cylinder and from the stationary plane wall forms a more complex wake structure and changes the flow stability conditions.

Most of the experiments for the flow around a cylinder over a plane wall were performed at Reynolds numbers in the subcritical regime ($300 \leqslant Re \leqslant 1.4 \times 10^5$) where the boundary layer along the cylinder surface is still laminar [14–23]. Lei et al. [22] and Price et al. [23] summarized well the experimental investigations into this problem. These studies have aimed at revealing the dependence of forces

* Corresponding author. Tel.: +82 51 510 3685; fax: +82 51 581 3718.
E-mail address: lesmodel@pusan.ac.kr (H.S. Yoon).

0017-9310/$ - see front matter © 2007 Elsevier Ltd. All rights reserved.
doi:10.1016/j.ijheatmasstransfer.2007.01.012

Nomenclature

c	space-averaged streamwise exit velocity
C_D	drag coefficient
C_L	lift coefficient
D	cylinder diameter
f	momentum forcing
G	gap between the cylinder and a moving wall
h	heat source/sink
n	normal direction to the wall
q	mass source/sink
Nu	local Nusselt number
$\langle Nu \rangle$	surface-averaged Nusselt number
$\langle \overline{Nu} \rangle$	time- and surface-averaged Nusselt number
p	pressure
Pr	Prandtl number
St	Strouhal number
t	time
t_p	period of time integration
T	temperature
T_s	cylinder surface temperature
T_∞	free-stream temperature
u, v	velocity components in x and y directions
U_∞	free-stream velocity
W	cylinder surface
x, y	Cartesian coordinates

Greek symbols

α	thermal diffusivity
β	thermal expansion coefficient
ρ	density
σ	electric conductivity
ν	kinematic viscosity
ω_w	wall vorticity

Sub/superscripts

max	maximum
min	minimum
rms	root mean square
–	time-averaged quantity

acting on the cylinder and vortex shedding frequency on the ratio G/D of the gap between the cylinder and the plane wall, G, and the cylinder diameter, D. They have also been concerned with understanding the effect on these quantities of the boundary layer thickness and the velocity gradient. Price et al. [23] briefly tabulated the drag coefficient, C_D, Strouhal number, St, and critical G/D to suppress vortex shedding according to previous experiments in company with the experimental conditions such as Reynolds number, G/D, the boundary thickness, and type of measure. Even in different experiments, the critical G/D to suppress vortex shedding ranges mainly between 0.2 and 0.4.

In contrast to the experiments, only a small number of literatures using numerical approach are available. Lei et al. [24] studied numerically the dependence of the critical Reynolds number on the gap ratio in the range of $80 \leqslant Re \leqslant 1000$. For $G/D < 0.2$, they showed that flow has a steady behavior up to $Re = 1000$. Zovatto and Pedrizzetti [13] confirmed the small gap ratio of Lei et al. [24] needed to suppress the vortex shedding by numerically analyzing flow around a cylinder positioned eccentrically between two lateral walls at $Re < 300$.

The purpose of this work is to numerically study the flow and heat transfer around a circular cylinder over a wall moving with the same velocity with the free-stream velocity. Thus, the effect of boundary layer thickness and the free-stream velocity profiles can be neglected. The present study limits the values of Reynolds number to below the critical value of about 194 [6] which causes the transition from two-dimensional to three-dimensional flow. Based on the authors' survey of literature considering the similar flow conditions in terms of Reynolds number and no boundary layer effect with those of present study, only one experiment by Taneda [25] has been found. Taneda [25] presented flow visualization at $Re = 170$, when the cylinder was moved in stagnant fluid close to a stationary wall, thus there were no boundary layer effects. He observed only a single row of vortices for $G/D = 0.1$ and a two-row vortex street for $G/D = 0.6$. Especially, it is hard to find that a literature has dealt with heat transfer problems of this subject.

As an initial stage of the study dealing with flow and heat transfer around a circular cylinder over a moving wall, the present study focus on providing the quantitative information about the flow and heat transfer variables such as the drag and lift coefficients, Strouhal number, the wall vorticity and Nusselt number within the specified gap ratios for different Reynolds numbers rather than searching for the accurate critical gap ratio to suppress the vortex shedding.

2. Computational details

The immersed boundary method is used to simulate flow and thermal fields over a circular cylinder near a moving wall. Therefore, the governing equations describing unsteady incompressible viscous flow and thermal fields in the present study are the momentum, continuity and energy equations:

$$\frac{\partial u_i}{\partial t} + \frac{\partial u_i u_j}{\partial x_j} = -\frac{\partial p}{\partial x_i} + \frac{1}{Re}\frac{\partial^2 u_i}{\partial x_j^2} + f_i \tag{1}$$

$$\frac{\partial u_i}{\partial x_i} - q = 0 \tag{2}$$

$$\frac{\partial T}{\partial t} + \frac{\partial u_j T}{\partial x_j} = \frac{1}{RePr}\frac{\partial^2 T}{\partial x_j^2} + h \tag{3}$$

where x_i are Cartesian coordinates, u_i are the corresponding velocity components, t is the time, p is the pressure, and T is the temperature. The momentum forcing f_i and mass source/sink q are applied on the body surface or inside the body to satisfy the no-slip condition and mass conservation the cell containing the immersed boundary. In Eq. (3), the heat source/sink h is applied to satisfy the iso-thermal boundary condition on the immersed boundary.

All the variables are non-dimensionalized by the cylinder diameter D, free-stream velocity U_∞ and cylinder surface temperature T_s. The above non-dimensionalization results in two dimensionless parameters: $Re = U_\infty D/\nu$ and $Pr = \nu/\alpha$ where ν and α are the kinematic viscosity and thermal diffusivity. In the simulations to be reported here the Prandtl number, Pr, has been taken to be 0.7 corresponding to air. The Reynolds numbers of $Re = 100$, 140 and 180 are considered.

A two-step time-split scheme is used to advance the flow field. This scheme is based on the previous works of Kim and Moin [26] and Zang et al. [27]. First the velocity is advanced from time level 'n' to an intermediate level '$*$' by solving the advection–diffusion equation without the pressure term. In the advection–diffusion step, the nonlinear terms are treated explicitly using third-order Adams–Bashforth scheme. The diffusion terms are treated implicitly using Crank–Nicolson scheme. Then the Poisson equation for pressure, which is derived by using mass conservation, is solved fully implicitly. Once the pressure is obtained, the final divergence-free velocity field at '$n+1$' is obtained with a pressure-correction step. The temperature field is advanced in a similar manner with third-order Adams–Bashforth scheme for the advection term and Crank–Nicolson scheme for the diffusion term.

The central difference scheme with the second-order accuracy based on the finite volume method is used for the spatial discretization. Additionally, a second-order linear or bilinear interpolation scheme is applied to satisfy the no-slip and iso-thermal conditions on the immersed boundary. Further details of the immersed-boundary method are given in Kim et al. [28] and Kim and Choi [29].

Fig. 1 shows the computational domain, coordinates system and grid distribution near the cylinder over a moving wall. The size of computational domain is $-50 \leqslant x \leqslant 50$ and $0 \leqslant y \leqslant 50$ for the streamwise and transverse directions, respectively. The gap ratio G/D has changed in eight cases having the values 0.1, 0.2, 0.3, 0.4, 0.5, 1, 2 and 4. Therefore, for the three Reynolds numbers studied, 24 cases in total are considered.

At the inflow, moving wall and far-field boundaries, the Dirichlet boundary conditions, $u = 1$, $v = 0$ and $T = 0$, are enforced. On the surface of the cylinder or immersed boundary, no-slip and no-penetration boundary conditions, $u = 0$ and $v = 0$, are imposed for the velocity field, while isothermal boundary condition, $T = 1$, is enforced for the temperature. The convective boundary conditions, $\partial u_i/\partial t + c\partial u_i/\partial x = 0$ and $\partial T/\partial t + c\partial T/\partial x = 0$, are applied

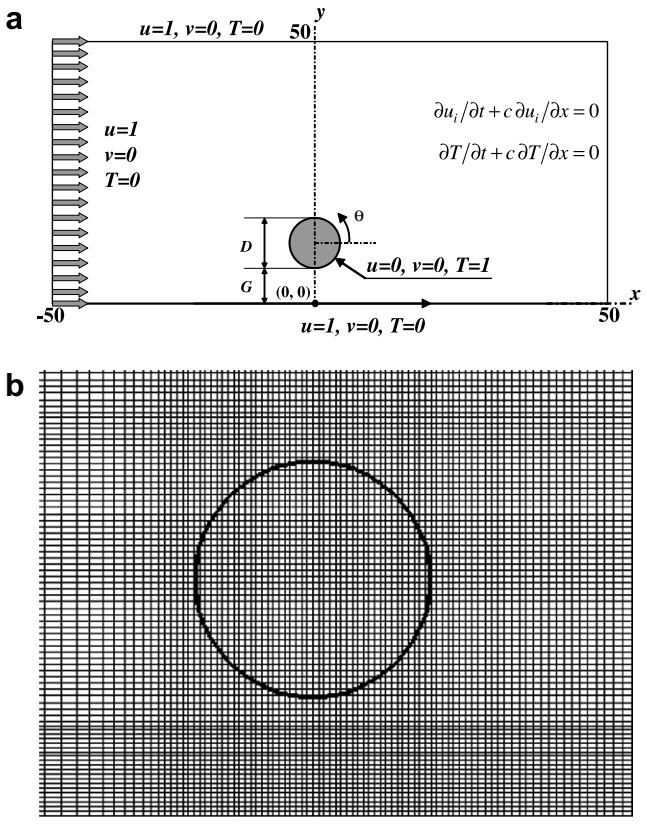

Fig. 1. (a) Computational domain and coordinate system along with boundary conditions, and (b) mesh near the cylinder over a moving wall.

at the outflow boundary, where c is the space-averaged streamwise exit velocity, u and v are the velocity components in x and y directions, respectively.

The number of total grid points used is $449(x) \times 253(y)$. The grids are non-uniformly distributed near the cylinder, especially in the gap and the wake region to accurately capture the separating shear layers around the cylinder and over the moving wall and in order to account for the high gradients near the walls. Sixty grid points in each direction are uniformly distributed within the cylinder while a hyperbolic tangent distribution is in the outer regions. In order to consider the variation of the gap ratio, the number of grid points used in the y-direction is tuned to maintain the dense resolution near the cylinder, moving wall and in the gap spacing. The grid refinement test is carried out for the smallest gap ratio of 0.1 and also largest gap ratio of 4 at $Re = 100$ and 180. Grid independence of the solution has been confirmed with additional simulations on the finer grids $(513(x) \times 301(y))$ changing the body forces and Nusselt number by less than 1%. The condition of CFL < 0.3 is chosen to determine the non-dimensional time step used in the present calculations. The computations were advanced in time until it was observed that the drag, lift and heat transfer coefficients have reached a statistically stationary state. Especially, for the small gap ratios, the effect of calculation time on the fully developed state has been examined using the different initial

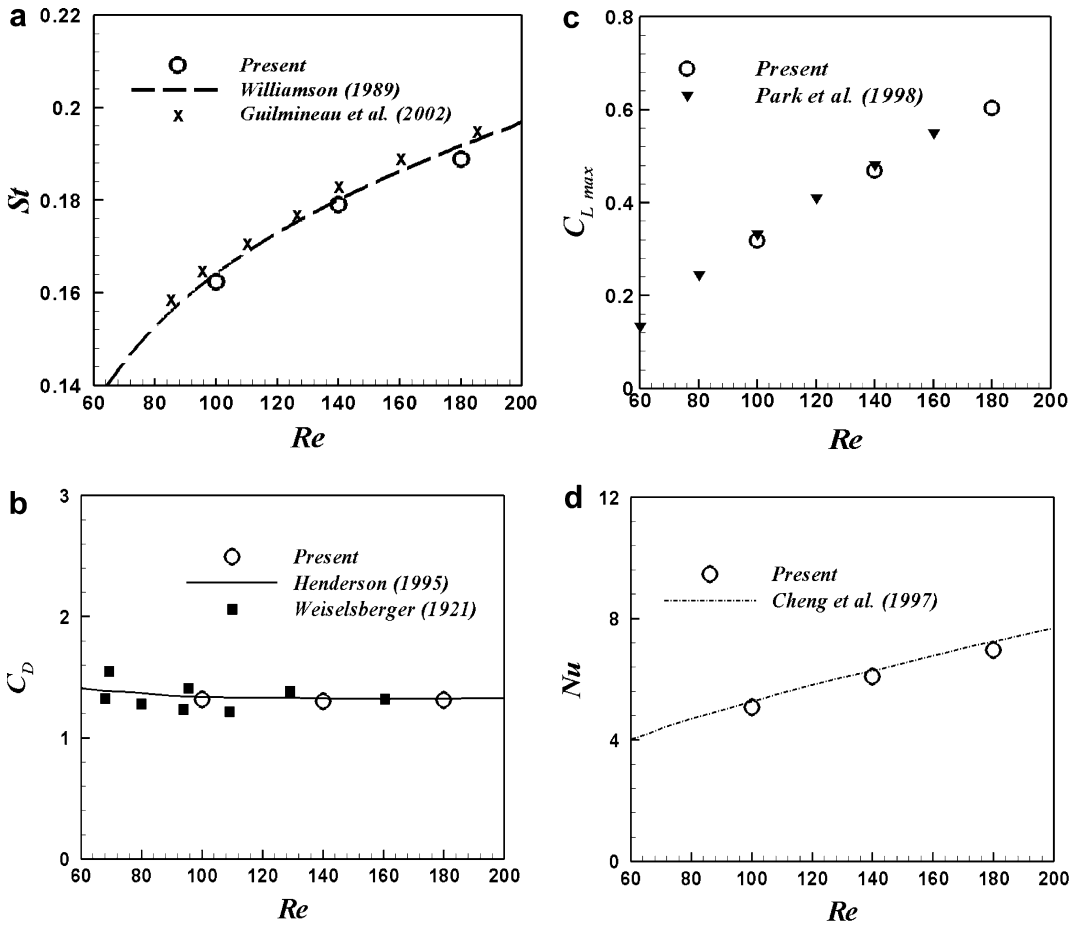

Fig. 2. Comparisons of the present study and references for the cases of an unbounded circular cylinder. (a) Strouhal number, (b) drag coefficient, (c) lift coefficient and (d) Nusselt number.

conditions. Although the simulations for the small gap ratios start with the different initial conditions, the fully developed steady or periodic flows are reached after about 50 time units. Every computation is extended to $t \geqslant 500$ to minimize the effect of calculation time on the final flow state.

Once the velocity and temperature fields are obtained, the local, surface-averaged, time-averaged, and time-and-surface-averaged Nusselt number are defined as

$$Nu = \left.\frac{\partial\theta}{\partial n}\right|_{\text{wall}} \quad \langle Nu\rangle = \frac{1}{W}\int_0^W Nu\,\mathrm{d}S \quad \overline{Nu} = \frac{1}{t_p}\int_0^{t_p} Nu\,\mathrm{d}t \quad \langle\overline{Nu}\rangle = \frac{1}{t_p}\int_0^{t_p}\langle Nu\rangle\,\mathrm{d}t \tag{4}$$

where n is the normal direction to the walls, W is the cylinder surface and t_p is the period of time integration.

The validation of present numerical method has been performed by the comparisons with previous results of experiments and computations for the unbounded circular cylinder as shown in Fig. 2a–d. The present Strouhal numbers at different Reynolds numbers agree well with those of previous experiment [5] and computation [30]. Drag and lift coefficients at corresponding Reynolds number are in good agreement with drag coefficient of Henderson [31] and Weiselsberger [32], and lift coefficient of Park et al. [33]. Also, present Nusselt numbers at different Reynolds numbers well match the numerical results of Cheng and Hong [34].

3. Results and discussion

3.1. Fluid flow

The instantaneous vorticity contours for different gap ratios of $G/D = 4$, 2, 1, 0.5, 0.4, 0.3, 0.2 and 0.1 at $Re = 100$ are shown in Fig. 3a–h, respectively. At the largest gap ratio of $G/D = 4$, the flow around the cylinder is in effect indistinguishable from that around an unbounded circular cylinder. The well-defined two-row street of vortices is formed with clockwise negative vortices shed from the upper side of cylinder and counter-clockwise positive ones shed from the opposite side of cylinder. However, it can be expected through the existence of wall vorticity over a moving wall that flow is undergone very weak effect of the gap flow. When $G/D = 2.0$, the wake behind a cylinder is still characterized as the two-row vortex street over the entire downstream region. This wake gives an effect on gen-

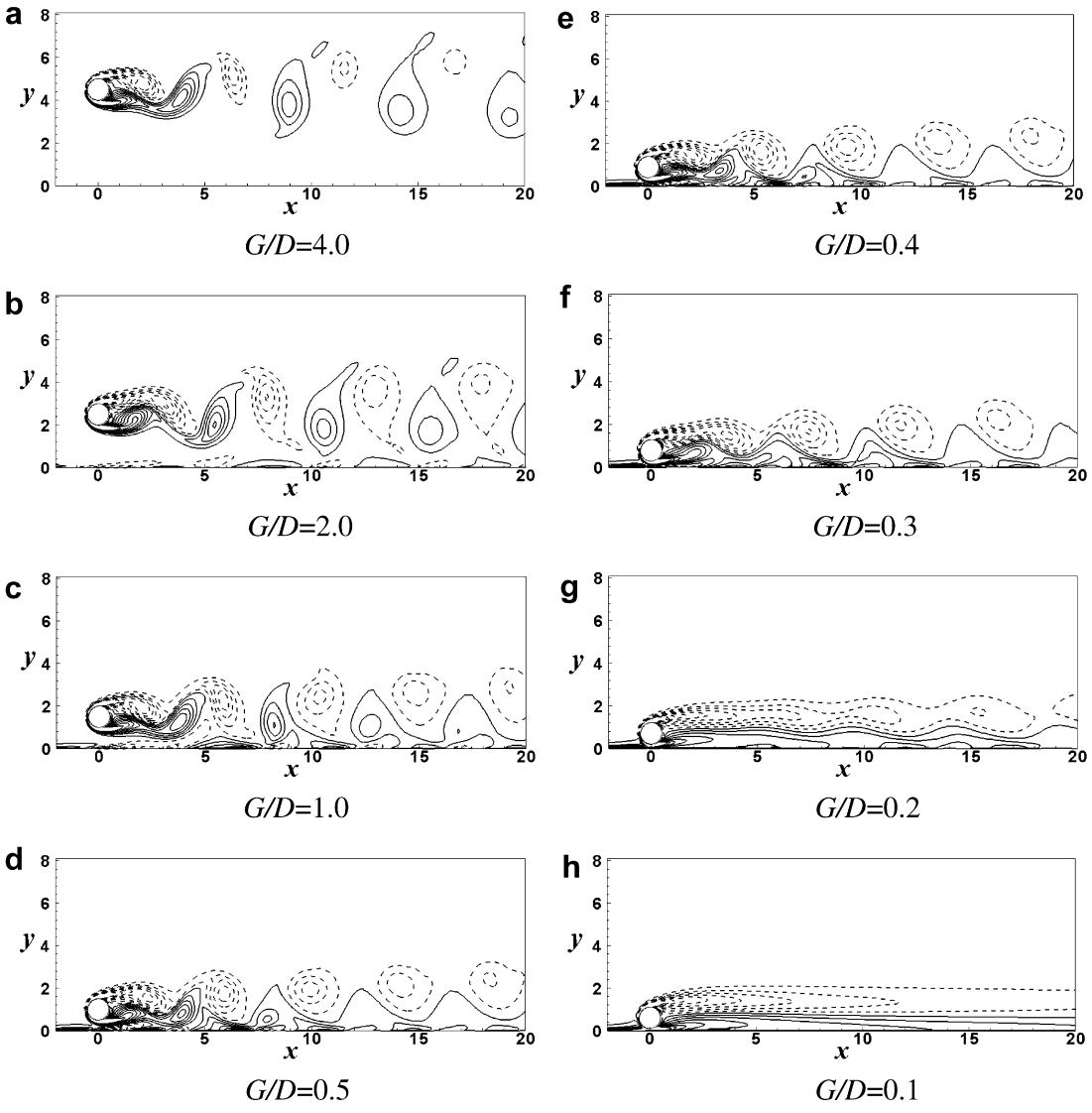

Fig. 3. Instantaneous vorticity contours for the different G/Ds of (a) 4, (b) 2, (c) 1, (d) 0.5, (e) 0.4, (f) 0.3, (g) 0.2 and (h) 0.1 at $Re = 100$ (contour values range from -3 to 3 with 16 levels).

erating wall shear layers, with alternative sign depending on vortex shed from the cylinder, over the moving wall.

Further decreasing the gap size, the positive vorticity shed from the wall side of the cylinder much strongly interacts with the boundary layer negative vorticity of the moving wall while the actual wake is dominated by the vorticity shed from opposite side of the cylinder. The vorticity shed from the wall side of the cylinder is stretched during the pairing with the opposite sign vorticity developed from the moving wall, which delays the roll up into a well-defined vortex and reduces the circulation of the eventual wake vortex because of the dissipative nature of the stretching process. Thus, with decrease in the gap, the region showing two-row vortex structure is gradually diminished from far downstream of cylinder. When the gap size reaches to $G/D = 0.5$, two-row vortex structure is eventually transformed into one-row structure as shown in Fig. 3d. This one-row structure associated with the shear-layer shed from the upper side of the cylinder is kept until to $G/D = 0.3$. At $G/D = 0.2$, vortex shedding in the wake region does not appear anymore. The wake vorticity on the upper side of the cylinder elongates farther downstream. When the wake is long enough it begins to fluctuate at the downstream tail. At the smallest gap ratio of $G/D = 0.1$, the flow is stabilized and the steady state with an asymmetric shape of vorticity along the cylinder centerline. The length of wake vorticity on the wall side is shorter than that of wake vorticity on the opposite side of the cylinder. The magnitude of streamwise velocity in the gap between the cylinder and moving wall is restricted to that of the moving wall velocity, and the vertical motion of flow in the region of gap is strongly inhibited by a moving wall. Thus, the gap flow between the cylinder and a moving wall is much weaker than flow over the upper side of cylinder.

With increasing Re, the wake vorticities on both sides of cylinder become shorter in length and stronger in

concentration in all the ranges of gap ratio, which can be identified by comparing the instantaneous vorticity contours for $Re = 100$, 140 and 180 in Figs. 3 and 4, respectively. Because the shear-layer developed from the wall and the shear-layer shed from the lower side of the cylinder couple and roll up, the flow at $Re = 140$ and 180 still shows a single row of vortices with a strong unsteadiness at $G/D = 0.2$ and 0.1, in contrast to that at $Re = 100$. This single vortex row was observed also in the flow visualization by the experiment of Taneda [25].

Fig. 5 shows the Strouhal number variation as a function of gap ratio at three different Reynolds numbers of 100, 140 and 180. The absolute Strouhal numbers and normalized Strouhal numbers in terms of the Strouhal number St_0 obtained at $G/D = 4$ are plotted in Fig. 5a and b, respectively, which shows the dependence of the Strouhal number on the gap ratio and Reynolds number. In the range of gap ratio considered in this study, the dependence of St on Reynolds number is analogous to that of unbounded cylinder. The Strouhal number variation along the gap ratio for three Reynolds numbers is almost the same pattern as follows. The value of Strouhal number increases with decreasing G/D up to 0.5 since the gap flow accelerates. As G/D continuously decreases, the value of Strouhal number decreases rapidly because the gap flow is stabilized by the wall effect.

For three different Reynolds numbers, the Strouhal number does not change significantly when G/D is larger than 2. The maximum variation of the Strouhal number in this gap range is less than 3% as shown in Fig. 5b. At $G/D = 0.5$, the Strouhal number has a maximum value with about a 12% augmentation relative to the largest gap ratio regardless of the Reynolds number variation. As the cylinder is moved further toward the moving wall below $G/D < 0.5$, the Strouhal number quickly decreases. As shown in Fig. 5b, decreasing ratio of the Strouhal number becomes large as

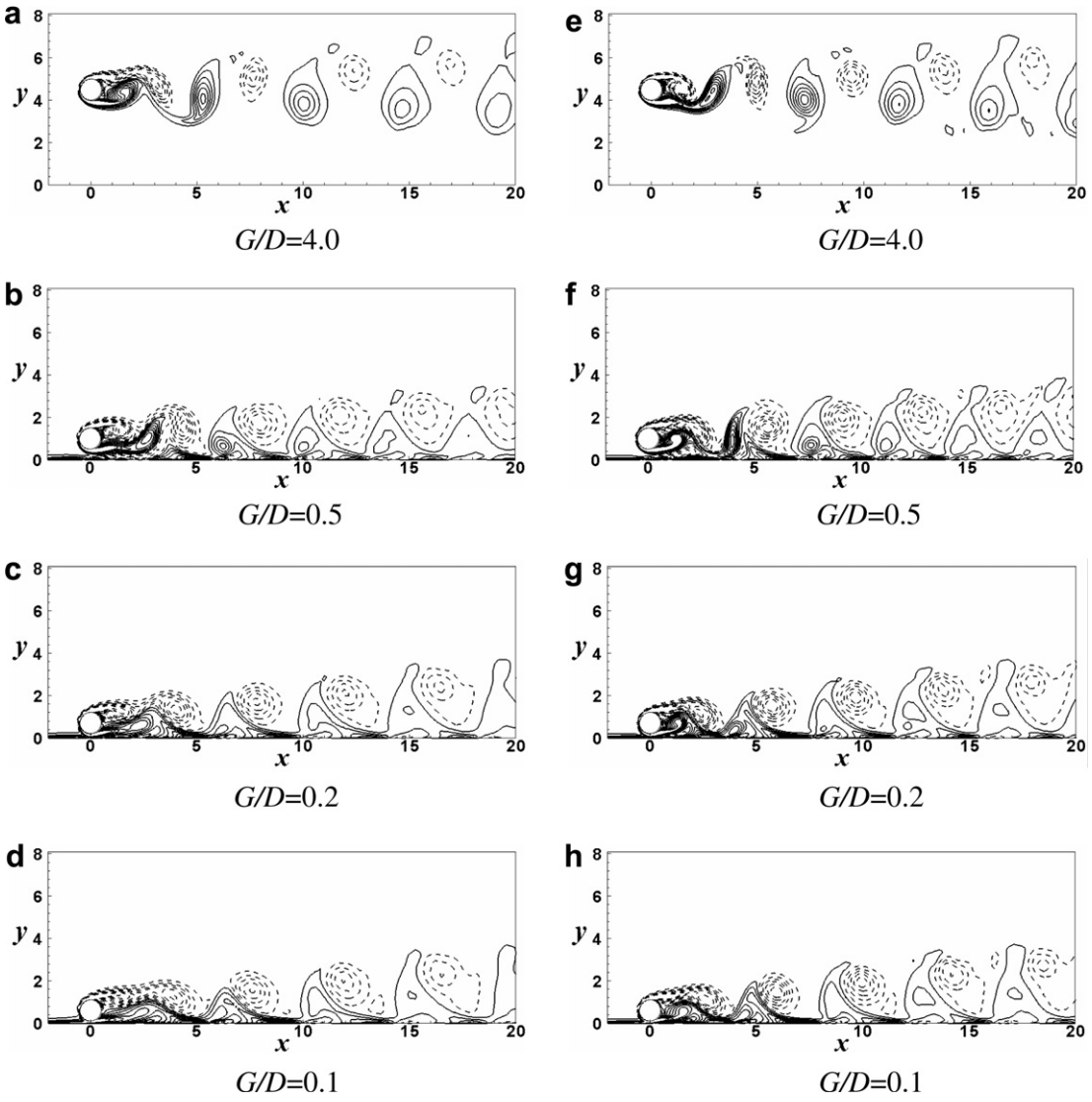

Fig. 4. Instantaneous vorticity contours for the different G/Ds of 4, 0.5, 0.2 and 0.1 at $Re = 140$ (a–d) and $Re = 180$ (e–h) (contour values range from −3 to 3 with 16 levels).

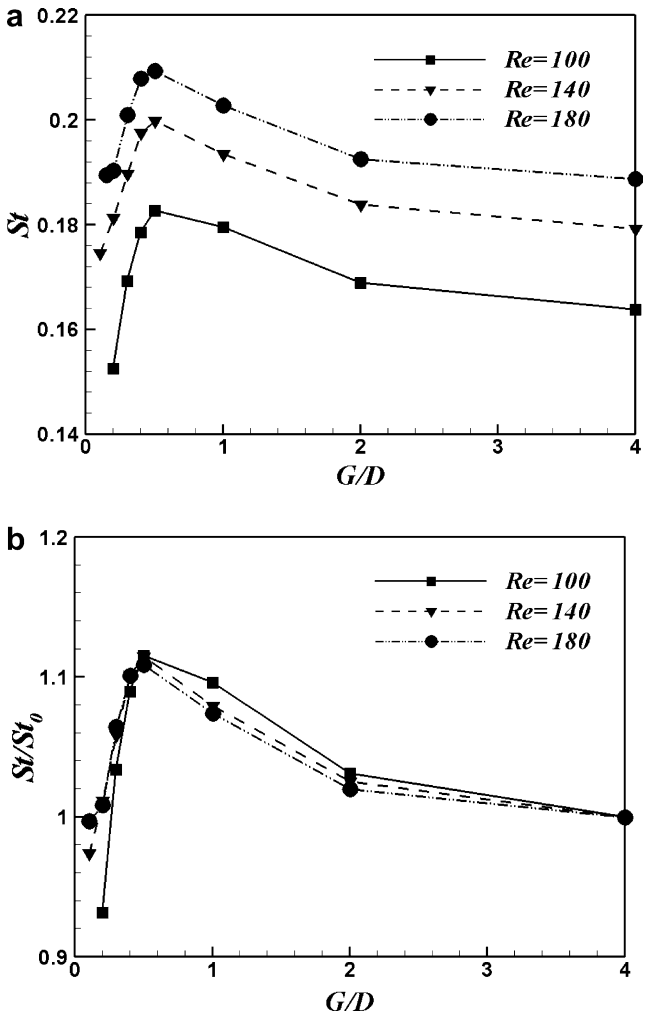

Fig. 5. Strouhal number as a function of gap ratio at three different Reynolds numbers of 100, 140 and 180; (a) absolute Strouhal numbers, (b) normalized Strouhal numbers in terms of the Strouhal number St_0 obtained at $G/D = 4$.

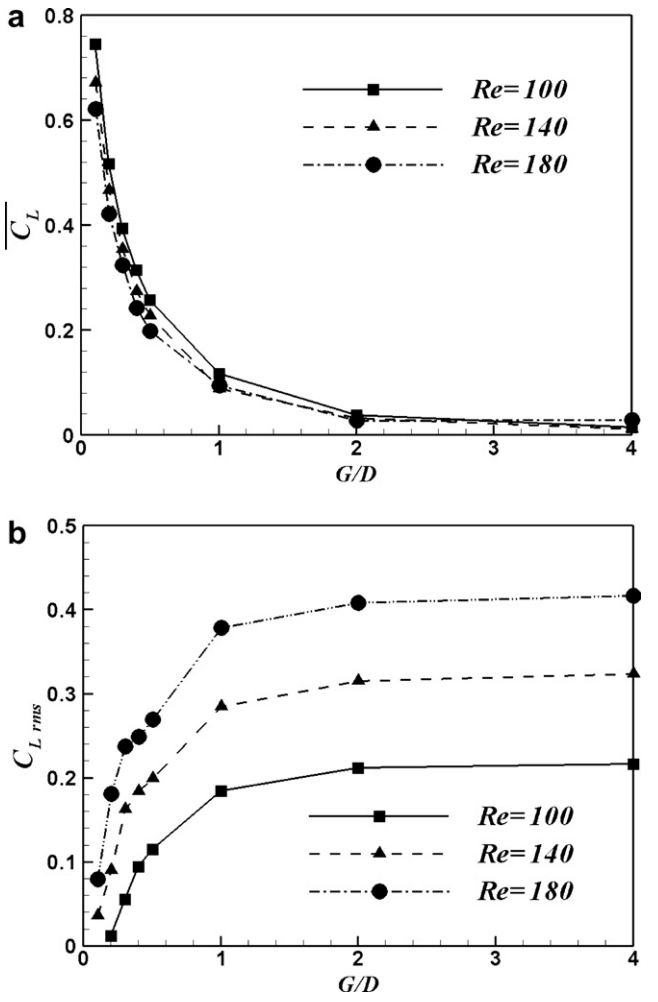

Fig. 6. (a) Time-averaged and (b) root-mean-square (RMS) values of lift coefficient as a function of gap ratio (G/D) for three different Reynolds numbers of 100, 140 and 180.

Reynolds number decreases. At the lowest $G/D = 0.1$ among the gap ratios considered in this study, the Strouhal number changes with less than 3% deviation from St_0 for both $Re = 140$ and 180. However, for $Re = 100$, the Strouhal number does not appear since flow is stabilized by the suppression of vortex shedding as shown in Fig. 3h. As a result the Strouhal number decreases rapidly with deceasing G/D, which is another evidence to prove that the flow is stabilized as the G/D decreases.

The time-averaged and root-mean-square (RMS) values of lift coefficient as a function of gap ratio for three different Reynolds numbers are plotted in Fig. 6a and b, respectively. It can be certified from Fig. 6a that a similar pattern of $\overline{C_L}$ variation according to the gap ratio happens at all the Reynolds numbers considered in this study.

At the largest gap ratio of 4.0, since the periodic vortex shedding from the top and bottom parts of the cylinder resembles the isolated cylinder case, the time-averaged lift coefficient ($\overline{C_L}$) reaches to almost zero value, meaning that instantaneous C_L regularly oscillating with nearly same positive maximum and negative minimum values based on zero. The front stagnation point moves toward the wall side of the cylinder with decreasing G/D, which can be clarified by the careful observation of the instantaneous vorticity contours plotted in Figs. 3 and 4 and the time-averaged wall vorticity along the cylinder surface shown later in Fig. 7. Consequently, as decreasing the gap ratio, the pressure under the bottom part of cylinder becomes much higher than that over the top part of cylinder and as a result $\overline{C_L}$ increases into the positive value. Even not shown in here, it can be observed from the time history of instantaneous C_L that the center of instantaneous C_L oscillating along the time gradually deviates from zero to positive value as decreasing G/D. When the cylinder is moved to the certain gap ratio depending on Reynolds number, the instantaneous C_L oscillates with only positive value. However, the magnitude of $\overline{C_L}$ decreases with increasing the Reynolds number, when a cylinder is moved further toward the wall. It can be supported from Fig. 6a that the dependence of $\overline{C_L}$ on Reynolds number is stronger as reducing the gap ratio.

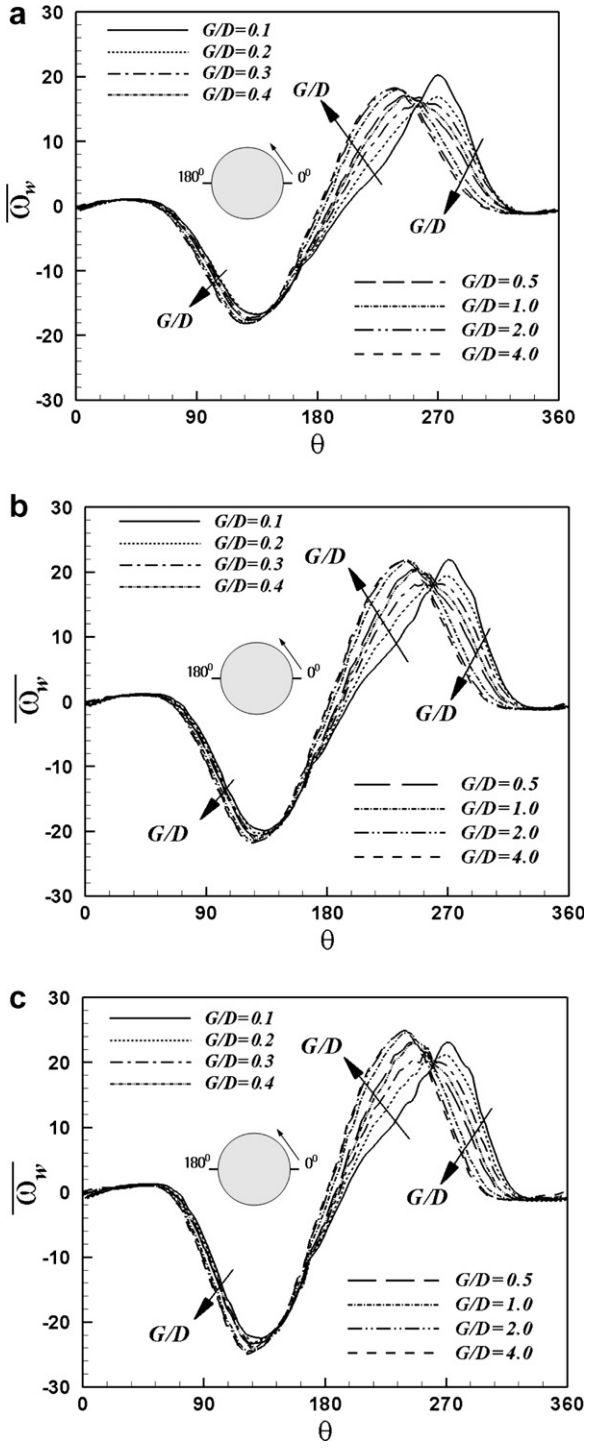

Fig. 7. Time-averaged wall vorticity as a function of circumferential direction θ at different gap ratios for (a) $Re = 100$, (b) 140 and (c) 180.

In the range of gap ratios between 0.1 and 4.0 considered in this study, RMS lift coefficient increases with the gap ratio, since the strength of vortex shedding increases with the gap ratio, and the wall effect on the vortex shedding becomes weaker and weaker. Especially, in the large gap ratios with constant RMS lift coefficient, the vortex shedding induced by flow separating from the top and bottom parts of the cylinder shows periodic pattern, because the wall effect is not significant.

As well known, the higher the Reynolds number, the stronger the vortex shedding. It means that the fluctuation of the lift is stronger at high Reynolds numbers. The turning gap ratio for the onset or suppression of the vortex shedding also depends on the Reynolds number. This gap ratio is higher in low Reynolds number flows, which can be identified by comparing the vorticity contours for different Reynolds numbers in Figs. 3 and 4. For $Re = 100$, there is no value of RMS lift at $G/D = 0.1$, because the oscillation of instantaneous C_L along the time disappears due to the regular vortex shedding completely suppressed as early shown in Fig. 3h.

Fig. 7 shows the time-averaged wall vorticity ($\overline{\omega_w}$) as a function of circumferential direction θ for different gap ratios at three different Reynolds numbers. Here, overbar $\overline{()}$ denotes the time-averaged quantity, and $\theta = 0^\circ$ and 180° represent the rear and front stagnation points of the unbounded cylinder as shown in Fig. 1.

The dependence of $\overline{\omega_w}$ on gap ratio is about the same for three Reynolds numbers. Namely, since the front stagnation point moves toward the wall side of the cylinder with decreasing G/D, flow consumes more kinetic energy to turn over from the front stagnation point located at the wall side of the cylinder to top part of cylinder and to overcome the increased viscous regime. Thus, when the cylinder approaches to the wall, the time-averaged wall vorticity around the top part of cylinder decreases and the circumferential location, $\theta_{\bar{\omega}_{w,max}}$, at which the wall vorticity $\overline{\omega_w}$ has a maximum value, is closer to the front stagnation point ($\theta = 180^\circ$) of unbounded cylinder flow.

Over the wall side of cylinder, as G/D decreases, the front stagnation point moves toward the bottom part of the cylinder, and consequently $\theta_{\bar{\omega}_{w,max}}$ moves to the downstream direction. However, the change of $\theta_{\bar{\omega}_{w,max}}$ is limited to $\theta = 270^\circ$ where the distance between the cylinder and the wall is minimum. Thus, the maximum value of $\overline{\omega_w}$ for the smaller gap ratios of $G/D \leqslant 0.2$ is obtained at about $\theta = 270^\circ$ as shown in Fig. 7a–c for three different Reynolds numbers. It can be expected at the smallest G/D of 0.1 that the magnitude of maximum value of $\overline{\omega_w}$ is dominated by the kinematic condition of the wall. Therefore, the magnitude of maximum value of $\overline{\omega_w}$ can be given by $|\bar{\omega}_{w,max} \sim U_{wall}/(G/D)|$ where U_{wall} is the wall velocity.

The acceleration of upstream flow near the bottom part of cylinder is restricted due to increasing flow resistance to the cross flow by the existence of the wall, which results in the decrease of $\overline{\omega_w}$ between the front stagnation point depending on G/D and $\theta \approx 260^\circ$ with decreasing G/D. In the circumferential range from $\theta \approx 260^\circ$ to the rear stagnation point depending on G/D, the magnitude of $\overline{\omega_w}$ increases with decreasing G/D as shown in Fig. 7a–c for three different Reynolds numbers.

The time-averaged drag coefficient as a function of the gap ratio for different Reynolds numbers of 100, 140 and 180 is shown in Fig. 8. $\overline{C_D}$ decreases for all gap ratios with

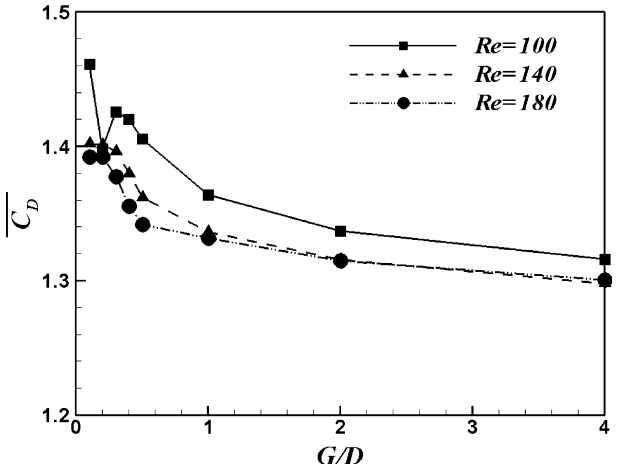

Fig. 8. Time-averaged drag coefficient as a function of gap ratio (G/D) for three different Reynolds numbers of 100, 140 and 180.

increasing Reynolds number. For $Re = 140$ and 180, the behavior of $\overline{C_D}$ has the same decaying pattern with increasing the gap ratio.

However, for $Re = 100$, the value of $\overline{C_D}$ undergoes a significant change in the gap ratios ranging from 0.1 to 0.3. In this range of the gap ratio, the flow transfers from the steady state to the unsteady state. At $G/D = 0.1$ corresponding to the steady flow, since the cylinder is almost submerged by the viscous boundary layers formed in between the bottom part of the cylinder and the moving wall as shown in Fig. 3h, the strong resistance occurs on the flow passing through the gap. Thus, $\overline{C_D}$ has a higher value at this gap ratio as shown in Fig. 8. However, at $G/D = 0.2$, the flow is going through the transition from the steadiness to very weak unsteadiness as shown in Fig. 3g. At this gap ratio, $\overline{C_D}$ is suddenly decreased because the increasing gap ratio reduces the flow resistance with

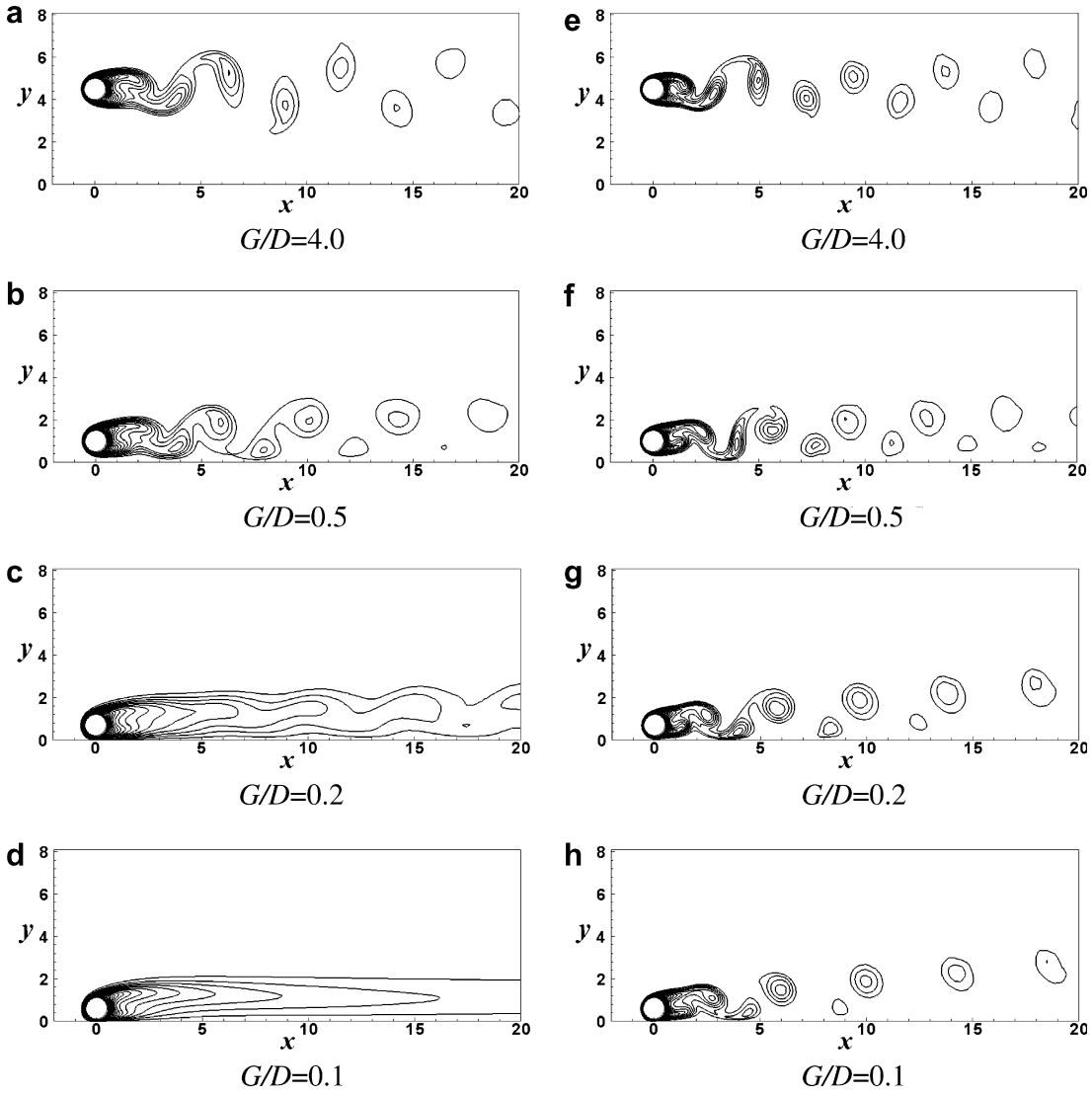

Fig. 9. Instantaneous temperature contours for the different G/Ds of 4, 0.5, 0.2 and 0.1 at $Re = 100$ (a–d) and $Re = 180$ (e–h) (contour values range from 0.09 to 1 with 19 levels).

diminishing the viscous gap and the vortex shedding is not appeared in the upper side of the cylinder. When the cylinder is located at $G/D = 0.3$, $\overline{C_D}$ increases again because the augmentation of $\overline{C_D}$ resulting from the appearance of vortex shedding in the upper side of the cylinder exceeds the drop of $\overline{C_D}$ due to the resistance reduction of flow passing through the gap with increasing the gap ratio. After $G/D > 0.3$, $\overline{C_D}$ gradually deceases with increasing the gap ratio.

3.2. Heat transfer

Fig. 9 shows the instantaneous temperature contours for the different gap ratios at $Re = 100$ and 180, respectively, which correspond to the instantaneous vorticity contours as shown in Figs. 3 and 4.

The change of thermal filed for various gap ratios and three different Reynolds numbers considered in this study can be explained by that of flow, because the thermal field as the passive scalar is governed by the flow. When $G/D = 4$, the isothermal lines are about the same as those of the unbounded cylinder for corresponding Reynolds number, which show the distribution of temperature concentration in response to well-defined two-row street of vortices.

When the cylinder is moved further toward the wall, the temperature contours below the wall side of the cylinder become much elongated and denser than those over the top part of the cylinder, because the vorticity separating from the wall side of the cylinder rolls up but is rapidly stretched by the wall vorticity of opposite sign.

But, in the case of $Re = 100$, thermal field stabilized except the downstream tail weak fluctuating at $G/D = 0.2$ and finally reaches to the steady state at $G/D = 0.1$ as shown in Fig. 9c and d, respectively, which follows the flow field as previously shown in Fig. 3g and h for the instantaneous vorticity contours at $G/D = 0.2$ and 0.1, respectively.

The time histories of surface-averaged Nusselt number $\langle Nu \rangle$ at different gap ratios for three different Reynolds numbers of 100, 140 and 180 are plotted in Fig. 10. For all gap values, it can be certified by comparing the time histories of $\langle Nu \rangle$ for $Re = 100$, 140 and 180 in Fig. 10a–c, respectively, that $\langle Nu \rangle$ and its oscillatory amplitude have the expected augmenting behavior with increasing Reynolds number. For all Reynolds numbers considered in this study, the variation of $\langle Nu \rangle$ shows the distinguished behavior at different ranges of G/D, because the flow and temperature fields have different distribution depending on G/D.

Within the range of $1 \leqslant G/D \leqslant 4$, $\langle Nu \rangle$s have almost the same oscillating amplitude and mean value. But, the secondary oscillation peak in the time variation of $\langle Nu \rangle$ becomes less and less as G/D decreases in this range, which is much significant with decreasing Reynolds number. This phenomenon is linked to the transition from the two-row vortex structure into one-row structure by which the vorticity in the separated free shear layer on the bottom part of cylinder becomes weak by interacting with the wall shear layer.

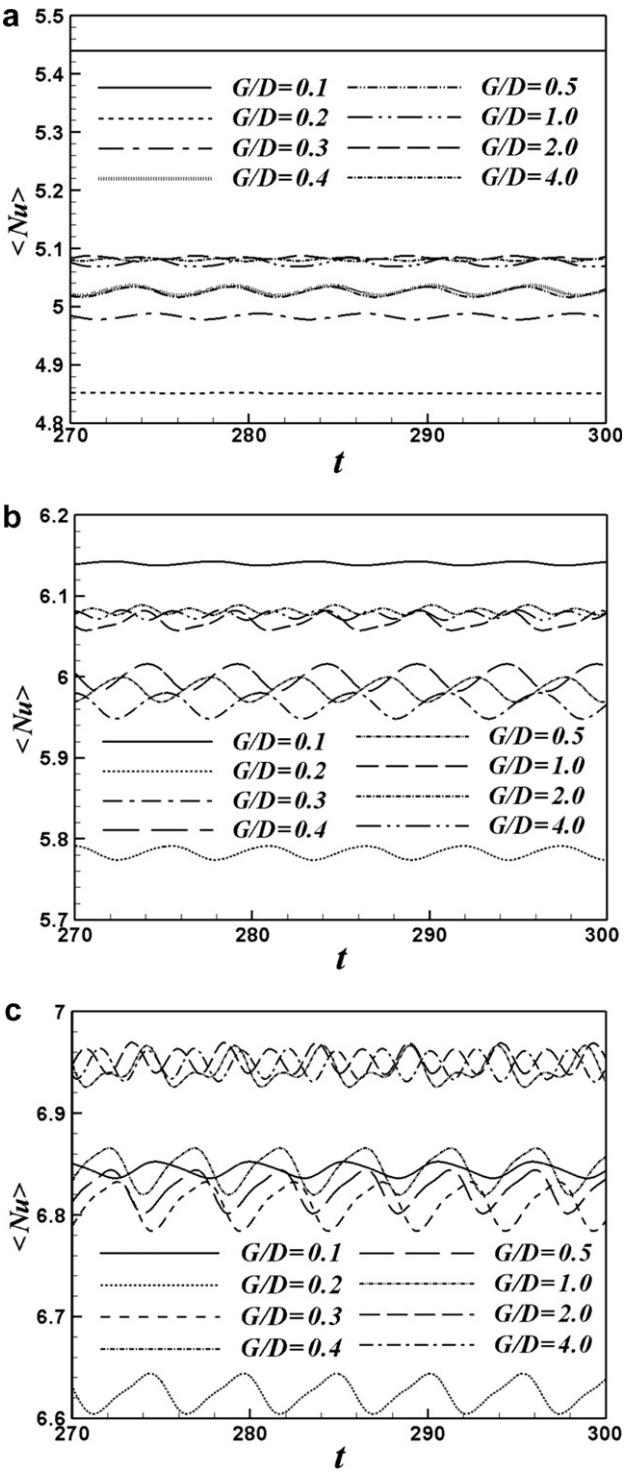

Fig. 10. Surface-averaged Nusselt number $\langle Nu \rangle$ as a function of the time at different gap ratios for three different Reynolds numbers of (a) 100, (b) 140 and (c) 180.

As G/D decreases at $0.3 \leqslant G/D \leqslant 0.5$ where the two-row vortex structure eventually falls into one-row structure for all Reynolds numbers, the value of $\langle Nu \rangle$ decreases. However, its oscillation amplitude is larger than that in

$1 \leqslant G/D \leqslant 4$, which is clearly shown with increasing the Reynolds number. In this range of G/D, the oscillation period of $\langle Nu \rangle$ is twice that of $\langle Nu \rangle$ in the range of $1 \leqslant G/D \leqslant 4$.

When G/D decreases to 0.2, $\langle Nu \rangle$ quickly decreases for all Reynolds numbers. At this gap ratio, the fluctuation of $\langle Nu \rangle$ shows the expected decaying behavior with decreasing Reynolds number. It has to be mentioned that the weak dependence of $\langle Nu \rangle$ on the time at $G/D = 0.2$ for $Re = 100$ looks like the steady state owing to the scale used to plot the time histories of $\langle Nu \rangle$ for all gap ratios.

When G/D decreases from 0.2 to 0.1, $\langle Nu \rangle$ increases rapidly for all Reynolds numbers. At this gap ratio, it can be expected from the Fig. 7 for the time-averaged local wall vorticity as a function of θ that the boundary layer thickness on the bottom part of cylinder facing close to the wall is significantly affected by the gap. In consequence, when the distribution of local Nusselt number at $G/D = 0.1$ is compared to that at $G/D = 4$, the increasing rate of local Nusselt number is larger than the decreasing rate of local Nusselt number and as a result $\langle Nu \rangle$ increases for $Re = 100$ and 140. The opposite is also true for $Re = 180$.

Fig. 11 shows the time-averaged temperature, $\bar{\theta}$ contours near the cylinder for the different gap ratios at $Re = 100$ and 180, respectively. For the gap ratios, the thickness of thermal boundary layer decreases with

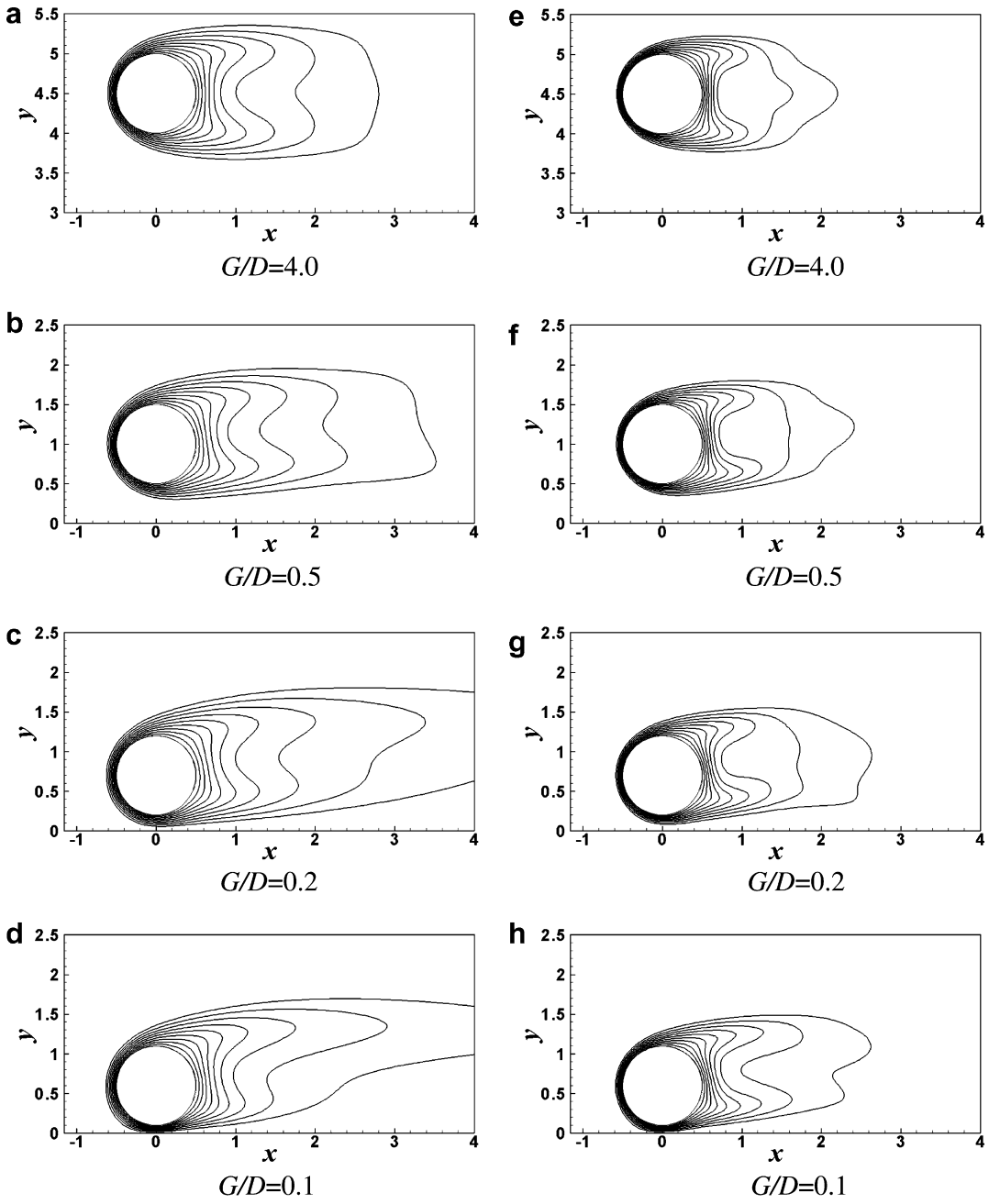

Fig. 11. Time-averaged temperature contours for the different G/Ds of 4, 0.5, 0.2 and 0.1 at $Re = 100$ (a–d) and $Re = 180$ (e–h) (contour values range from 0.1 to 1 with 10 levels).

increasing the Reynolds number, which can be observed by comparing the $\bar{\theta}$ contours of each corresponding gap ratio. For the Reynolds numbers, when the cylinder is approaching to the wall, the pattern of a change in $\bar{\theta}$ contours is generally the same as follows.

In the range of $1 \leqslant G/D \leqslant 4$, the distribution of $\bar{\theta}$ contours is almost the same as the unbounded cylinder case. When the cylinder further approaches the wall, wake on the wall side is weaker than that on the opposite side and the wall generally produces a repulsive force creating positive lift from it. Consequently, $\bar{\theta}$ contours temperature contours in the downstream region are inclined upward from the wall and as a result the distribution of temperature contours is asymmetric with respect to the x-axis crossing the cylinder center.

Fig. 12 shows the time-averaged local Nusselt number, $\overline{Nu}$, as a function of circumferential direction θ at different gap ratios for three different Reynolds numbers. The distribution of $\overline{Nu}$ has a deep relation with that of wall vorticity $\overline{\omega_w}$ as shown in Fig. 7. On the top part of the cylinder, if the wall vorticity increases with increasing G/D, the thermal boundary layer thickness decreases and as a result $\overline{Nu}$ increases. The opposite is also true. On this part of the cylinder, irrespective of the gap ratio, the distribution of $\overline{Nu}$ as a function of θ shows the similar pattern that $\overline{Nu}$ has a maximum value at $\theta = 180^{\circ}$ corresponding to the front stagnation point of the unbounded cylinder and decrease as we move from the stagnation to separation point depending on the gap ratio.

On the bottom part of the cylinder, as expected, the effect of the gap ratio on $\overline{Nu}$ is much strongly than that on the top part of the cylinder. As decreasing the gap ratio, $\overline{Nu}$ starts to increase when θ is approaching to the nearest location of $\theta = 270^{\circ}$ between the cylinder and the wall. Especially, at the smallest gap ratio of 0.1, the peak of $\overline{Nu}$ is located at $\theta = 270^{\circ}$ where the wall vorticity has the peak as shown in Fig. 7.

$\overline{Nu}$ increases for the gap ratios with increasing Reynolds number, because the thickness of forced convective thermal boundary layer decreases with increasing the Reynolds number. In the wall side of the cylinder, when the cylinder is getting much close to the wall and the Reynolds number is getting smaller, heat transfer will be dominate by the conduct mode. Thus, the dependence of $\overline{Nu}$ on the Reynolds number at $G/D = 0.1$ is very weak in the range of $250^{\circ} \leqslant \theta \leqslant 320^{\circ}$ where $\overline{Nu}$ rapidly increases and decreases.

At the lowest Reynolds number of 100 among the Reynolds numbers considered in this study, the maximum value of $\overline{Nu}$ for $G/D = 0.1$, which is located at $\theta = 270^{\circ}$, is larger than that of $G/D = 4$ at the front stagnation point as shown in Fig. 12a. As the result of this, it seems possible that the heat transfer in the region close to the wall by the conduct mode at $G/D = 0.1$ overcomes that induced by mainly convective mode at $G/D = 4$. However, when Re increases to 140 and 180, the maximum value of $\overline{Nu}$ at the front stagnation point for $G/D = 4$ is larger than that at $\theta = 270^{\circ}$ for $G/D = 0.1$ as shown in Fig. 12b and c.

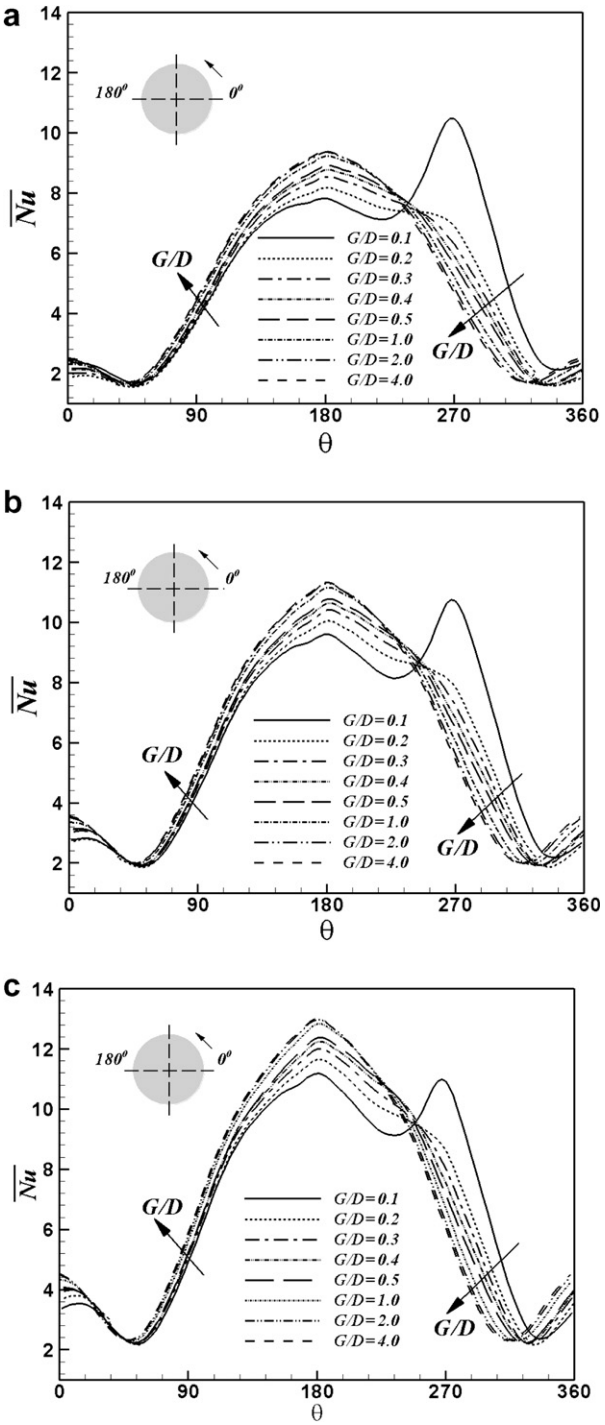

Fig. 12. Time-averaged local Nusselt number, $\overline{Nu}$, as a function of circumferential direction θ at different gap ratios for (a) $Re = 100$, (b) 140 and (c) 180.

Fig. 13 shows the time and surface-averaged Nusselt number, $\langle\overline{Nu}\rangle$, as a function of the gap ratio G/D for the three different Reynolds numbers of 100, 140 and 180. The absolute Nusselt numbers and normalized Nusselt numbers in terms of the Nusselt number $\langle\overline{Nu_0}\rangle$ obtained at $G/D = 4$ are plotted in Fig. 13a and b, respectively, which shows the dependence of the Nusselt number on the gap ratio and the Reynolds number. The behavior of

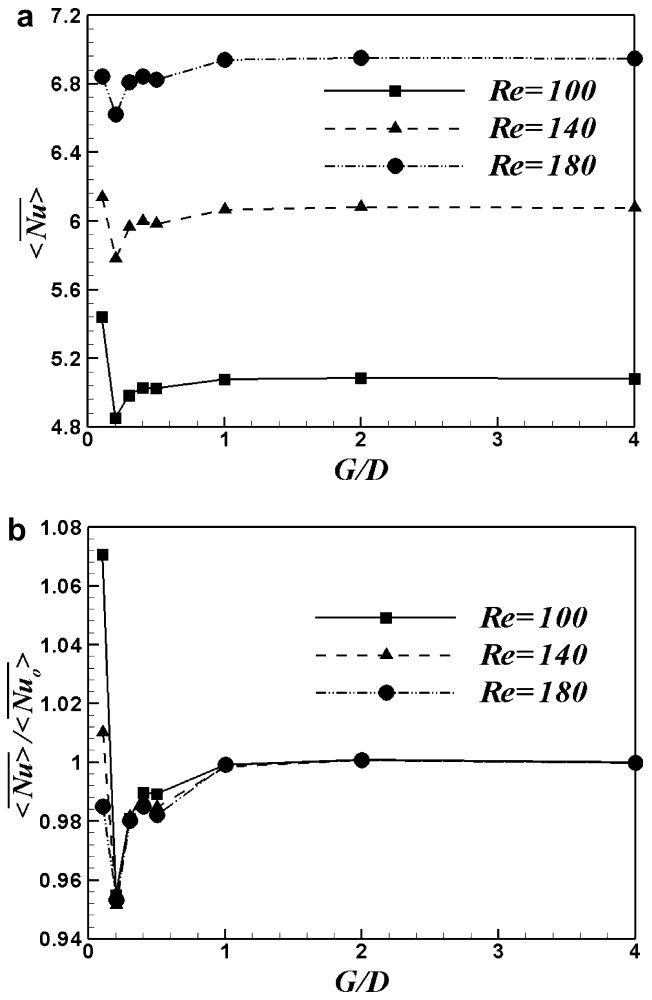

Fig. 13. Time and surface-averaged Nusselt number, $\langle\overline{Nu}\rangle$, as a function of the gap ratio G/D for the three different Reynolds numbers of 100, 140 and 180. (a) Absolute Nusselt numbers, (b) Normalized Nusselt numbers in terms of the Nusselt number $\langle\overline{Nu_0}\rangle$ obtained at $G/D = 4$.

$\langle\overline{Nu}\rangle$ for the gap ratios and Reynolds numbers can be estimated from the circumferential distribution of time-averaged local Nusselt number, $\overline{Nu}$, as shown in Fig. 12. The value of $\langle\overline{Nu}\rangle$ for all gap ratios shows the decaying behavior with decreasing Reynolds number.

For each Reynolds number, the variation of $\langle\overline{Nu}\rangle$ depending on the gap ratio is about the same pattern as follows. $\langle\overline{Nu}\rangle$ keeps a constant in the range of $1 \leqslant G/D \leqslant 4$. As G/D decreases in the range of $0.3 \leqslant G/D < 1$, the value of $\langle\overline{Nu}\rangle$ alternates a slight reduction and augmentation of about 2% for that at $G/D = 4$ as clearly shown in Fig. 13b. When the cylinder reaches to $G/D = 0.2$, $\langle\overline{Nu}\rangle$ decreases rapidly and has a minimum value because the decreasing rate of local Nusselt number $\overline{Nu}$ is larger than the increasing rate of $\overline{Nu}$ as shown in Fig. 12 for three different Reynolds numbers. At this gap ratio of 0.2, the rate of $\langle\overline{Nu}\rangle$ to that at $G/D = 4$ for three different Reynolds numbers has almost the same value which is about 4.5% less than that for $G/D = 4$. As G/D is decreased to 0.1, $\langle\overline{Nu}\rangle$ increases quickly. However, at this gap ratio, the dependence of Reynolds number on $\langle\overline{Nu}\rangle/\langle\overline{Nu_0}\rangle$ is much significant than other gap ratios as shown in Fig. 13b. For $Re = 100$ and 140, the values of $\langle\overline{Nu}\rangle$ at $G/D = 0.1$ are about 7% and 1% larger than those for $G/D = 4$, respectively. In contrast, for $Re = 180$, the value of $\langle\overline{Nu}\rangle$ at $G/D = 0.1$ is about 1.5% less than that for $G/D = 4$.

4. Conclusions

The present study numerically investigates the characteristics of two-dimensional laminar flow and heat transfer past a circular cylinder near a moving wall. In a second-order accurate finite volume method, an immersed boundary method for solving the Navier–Stokes and thermal energy equations is adopted to calculate the flow and heat transfer over a circular cylinder in the Cartesian coordinates. Comparisons with the published references show excellent agreement in detecting the drag, the lift, Strouhal number and Nusselt number of the unbounded cylinder for different Reynolds numbers considered in this study.

The flow and heat transfer are computed at a various range of gap ratios, $0.1 \leqslant G/D \leqslant 4$, for three different Reynolds numbers of 100, 140 and 180. A moving wall with the same velocity to the free-stream velocity guarantees the effect of boundary layer thickness and the free-stream velocity profiles in the front of a cylinder to be neglected.

For low Reynolds number of 100, at $G/D = 0.2$, no vortex shedding in the wake region is found. At $G/D = 0.1$, the flow reaches the steady state with an asymmetric shape of vorticity along the cylinder centerline. With increasing Reynolds number to 140 and 180, flow still shows a single row of vortices with the strong unsteadiness at $G/D = 0.2$ and 0.1. Based on this result, it can be concluded that the gap effect on flow stabilization is stronger at the lower Reynolds number.

As the cylinder is approaching the moving wall, the Strouhal number corresponding to vortex shedding frequency for all three Reynolds numbers slightly increases until to reach a maximum at $G/D = 0.5$ where the transition form two-row to single-row of vortices seems to be occurred, and then decreases rapidly. The lift increases with decreasing gap ratio and Reynolds number. In contrast, the RMS lift decreases with decreasing the gap ratio and Reynolds number.

With decreasing the gap ratio, the local peak of wall vorticity and Nusselt number along the cylinder surface moves to the downstream region. For the smaller gap ratios, especially, the local peak is located at the closest location between the cylinder bottom and the moving wall.

The value of time and surface-averaged Nusselt number for all gap ratios shows the decaying behavior with decreasing Reynolds number. For each Reynolds number, the dependence of time- and surface-averaged Nusselt number on the gap ratio is about the same pattern. At $G/D = 0.2$, the time- and surface-averaged Nusselt number for all three Reynolds numbers has the minimum value with the slight reduction of about 2% for the result at $G/D = 4$. As the Reynolds number decreases, the time and surface-averaged

Nusselt number significantly increases at the smallest gap ratio of 0.1.

Acknowledgment

This work was supported by Advanced Ship Engineering Research Center (ASERC) of Pusan National University through Korea Science and Engineering Foundation.

References

[1] R.A. Ahmad, Steady-state numerical solution of the Navier–Stokes and energy equations around a horizontal cylinder at moderate Reynolds numbers from 100 to 500, Heat Transfer Eng. 17 (1996) 31–80.
[2] M. Braza, P. Chassaing, H.H. Minh, Numerical study and physical analysis of the pressure and velocity fields in the near wake of a circular cylinder, J. Fluid Mech. 165 (1986) 79–130.
[3] R. Mittal, S. Balachandar, Direct numerical simulation of flow past elliptic cylinders, J. Comput. Phys. 124 (1994) 351–367.
[4] H.S. Yoon, H.H. Chun, M.Y. Ha, H.G. Lee, A numerical study on the fluid flow and heat transfer around a circular cylinder in an aligned magnetic field, Int. J. Heat Mass Transfer 47 (2004) 4075–4085.
[5] C.H.K. Williamson, Oblique and parallel modes of vortex shedding in the wake of a circular cylinder at low Reynolds numbers, J. Fluid Mech. 206 (1989) 579–628.
[6] C.H.K. Williamson, Vortex dynamics in the cylinder wake, Ann. Rev. Fluid Mech. (1996) 477–539.
[7] C.H.K. Williamson, Three-dimensional wake transition, J. Fluid Mech. 328 (1996) 345–407.
[8] K. Noto, K. Fujimoto, Formulation and numerical methodology for three-dimensional wake of heated circular cylinder, Numer. Heat Transfer, Part A 49 (2006) 129–158.
[9] S.K. Wang, T.C. Hung, G.W. Lin, B.S. Pei, Numerical simulations for the phenomena of vortex-induced vibration and heat transfer of a circular cylinder, Numer. Heat Transfer, Part A 45 (2004) 719–736.
[10] S. Singh, G. Biswas, A. Mukhopadhyay, Effect of thermal buoyancy on the flow through a vertical channel with a built-in circular cylinder, Numer. Heat Transfer, Part A 34 (1998) 769–789.
[11] M.S. Phanikumar, R.L. Mahajan, Numerical analysis of unsteady thermosolutal convection over a horizontal isothermal circular cylinder, Numer. Heat Transfer, Part A 33 (1998) 673–700.
[12] R. Bradean, D.B. Ingham, P.J. Heggs, I. Pop, Unsteady free convection adjacent to an impulsively heated horizontal circular cylinder in porous media, Numer. Heat Transfer, Part A 32 (1997) 325–346.
[13] L. Zovatto, G. Pedrizzetti, Flow about a circular cylinder between parallel walls, J. Fluid Mech. 440 (2001) 1–25.
[14] P.W. Bearman, M.M. Zdravkovich, Flow around a circular cylinder near a plane boundary, J. Fluid Mech. 89 (1978) 33–47.
[15] G. Buresti, A. Lanciotti, Vortex shedding from smooth and roughened cylinders in cross-flow near a plane surface, Aeronaut. Quarter. 30 (1979) 305–321.
[16] M.M. Zdravkovich, Intermittent flow separation from flat plate induced by a nearby circular cylinder, in: W. Merzkirch (Ed.), Proceedings of the 2nd International Symposium on Flow Visualization, Bochum, West Germany, 1980, pp. 265–270.
[17] M.M. Zdravkovich, Observation of vortex shedding behind a towed circular cylinder near a wall, in: Proceedings of the 3rd International Symposium on Flow Visualization, Ann Arbor, Michigan, 1983, pp. 391–395.
[18] M.M. Zdravkovich, Forces on a circular cylinder near a plane wall, Appl. Ocean Res. 7 (1985) 197–201.
[19] F. Angrilli, S. Bergamaschi, V. Cossalter, Investigation of wall induced modifications to vortex shedding from a circular cylinder, ASME J. Fluids Eng. 104 (1982) 518–522.
[20] A.J. Grass, P.W.J. Raven, R.J. Stuart, J.A. Bray, The influence of boundary layer velocity gradient and bed proximity on vortex shedding from free spanning pipelines, ASME J. Energy Resour. Tech. 106 (1984) 70–78.
[21] S. Taniguchi, K. Miyakoshi, Fluctuating fluid forces acting on a circular cylinder and interference with a plane wall, Exps. Fluids 9 (1990) 197–204.
[22] C. Lei, L. Cheng, K. Kavanagh, Re-examination of the effects of a plane boundary on force and vortex shedding of a circular cylinder, J. Wind Eng. Ind. Aer. 80 (1999) 263–286.
[23] S.J. Price, D. Sumner, J.G. Leong, M.P. Paidoussis, Flow visualization around a circular cylinder near to plane wall, J. Fluids Struct. 16 (2002) 175–191.
[24] C. Lei, L. Cheng, S.W. Armfield, K. Kavanagh, Vortex shedding suppression for flow over a circular cylinder near a plane boundary, Ocean Eng. 27 (2000) 1109–1127.
[25] S. Taneda, Experimental investigation of vortex streets, J. Phys. Soc. Jpn. 20 (1965) 1714–1721.
[26] J. Kim, P. Moin, Application of a fractional step method to incompressible Navier–Stokes equations, J. Comp. Phys. 59 (1985) 308–323.
[27] Y. Zang, R.L. Street, J.R. Koseff, A non-staggered grid, fractional step method for time-dependent incompressible Navier–Stokes equations in curvilinear coordinates, J. Comp. Phys. 114 (1994) 18–33.
[28] J. Kim, D. Kim, H. Choi, An immersed-boundary finite volume method for simulations of flow in complex geometries, J. Comp. Phys. 171 (2001) 132–150.
[29] J. Kim, H. Choi, An immersed-boundary finite-volume method for simulation of heat transfer in complex geometries, KSME Int. J. 18 (2004) 1026–1035.
[30] E. Guilmineau, P. Queutey, A numerical simulation of vortex shedding from an oscillating circular cylinder, J. Fluids Struct. 16 (2002) 773–794.
[31] R.D. Henderson, Details of the drag curve near the onset of vortex shedding, Phys. Fluids 6 (1995) 3677–3682.
[32] C. Wieselsberger, Neure festellungen uber die gesetze des flussigkeits- und luftwiderstands, Phys. Z. 22 (1921) 321–328.
[33] J. Park, K. Kwon, H. Choi, Numerical solution of flow past a circular cylinder at Reynolds number up to 160, KSME Int. J. 12 (1998) 1200–1205.
[34] C.H. Cheng, J.L. Hong, Numerical prediction of lock-on effect on convective heat transfer from a transversely oscillating circular cylinder, Int. J. Heat Transfer 40 (1997) 1825–1834.